Chemical Science

ROYAL SOCIETY OF CHEMISTRY

EDGE ARTICLE

View Article Online
View Journal | View Issue

Cite this: *Chem. Sci.*, 2024, **15**, 18952

All publication charges for this article have been paid for by the Royal Society of Chemistry

Received 21st June 2024
Accepted 13th October 2024

DOI: 10.1039/d4sc04105d

rsc.li/chemical-science

Visible light mediated photocatalysis by lanthanide metal–organic frameworks: enhanced specificity and mechanistic insights†

Ruchika Gupta,[a] Aashish,[a] Upma,[a] Shubhangi Majumdar,[b] Pramit K. Chowdhury [b] and Rajeev Gupta *[a]

The utilization of earth-abundant photosensitizers with visible light absorption to enable sustainable photocatalysis is a long-standing challenge. Overcoming such a challenge, in this work, two lanthanide (Ln^{3+} = Tb, Eu) based metal–organic frameworks (Ln-MOFs) have been synthesized utilizing a Co^{3+}-based metalloligand. Both Ln-MOFs function as remarkable photocatalysts for the selective oxidation of assorted alcohols and sulfides to their corresponding aldehydes/ketones and sulfoxides using visible light. The photophysical behavior of both Ln-MOFs and mechanism of photocatalysis is comprehensively investigated using time-resolved transient absorption spectroscopy, electrochemical impedance spectroscopy, electron paramagnetic resonance spectroscopy, photoluminescence and phosphorescence studies. In both Ln-MOFs, a metalloligand acts as a light-harvester, being excited by visible light, while Ln^{3+} ions endow the resulting MOFs with long-lived triplet excited states. Ultrafast transient absorption spectroscopy, further supported by electron paramagnetic resonance spectra, revealed excited-state electron transfer from metalloligands to the Ln^{3+} ions and transient generation of Ln^{2+} sites alongside the facilitation of intersystem crossing. The excited Ln^{2+} ions transfer energy to the ground-state triplet oxygen ($^3O_2$) to generate singlet oxygen ($^1O_2$). The HOMO–LUMO positions of both Ln-MOFs support the generation of $^{\bullet}O_2^-$ and $^1O_2$ but inhibit strongly-oxidizing yet non-selective $^{\bullet}OH$ radicals. Scavenger experiments, $^1O_2$ traps and electron paramagnetic resonance spectra confirmed the generation of singlet oxygen. The heavy-metal effect of a lanthanide ion in Ln-MOFs for the generation of triplet excitons is confirmed by the synthesis of a non-heavy-metal analogue involving a zinc ion *via* a single-crystal-to-single-crystal transformation strategy. The present results are noteworthy and may aid in the development of other earth-abundant metalloligand-based photocatalysts for challenging yet sustainable catalysis.

Introduction

Solar energy has emerged as a promising alternative to conventional fossil fuels and significant efforts are being made to utilize this sustainable source for myriad applications including chemical synthesis.[1–3] Among various visible-light catalyzed reactions, selective oxidation of organic compounds is immensely important.[4,5] However, most common organic compounds do not absorb light in the visible region, which accounts for nearly 47% of the solar spectrum.[6–8] This has significantly restricted the direct utilization of visible light in organic transformations.[6–8] However, this challenge has also opened new avenues and approaches to design and develop suitable catalysts to enable the use of visible light to drive chemical reactions.[1–3,9–14] One such approach is to activate a target reaction *via* charge-transfer catalysis mediated by a photosensitizer.[8,15,16] Typical photosensitizers include conjugated organic molecules; metal oxides, sulfides and phosphides; and coordination and organometallic complexes.[15–20] Previously, polypyridyl complexes of ruthenium and iridium have been extensively used as visible-light photosensitizers for several photochemical reactions due to their absorption in the visible region and superior excited-state lifetimes.[17–23] Despite remarkable achievements, progress is still limited with such photocatalysts due to the use of precious metals, homogeneous nature of catalysis, and limited reusability.[21–24] From a sustainability perspective, immobilization of such photocatalysts into solid materials to develop heterogeneous catalysts has also been explored but with limited success.[25–28]

Metal–organic frameworks (MOFs) have attracted significant interest as they offer several notable features including

[a]*Department of Chemistry, University of Delhi, Delhi 110 007, India. E-mail: rgupta@chemistry.du.ac.in; Web: https://people.du.ac.in/~rgupta/*

[b]*Department of Chemistry, Indian Institute of Technology, Delhi, India*

† Electronic supplementary information (ESI) available. CCDC 2288468 and 2288469. For ESI and crystallographic data in CIF or other electronic format see DOI: https://doi.org/10.1039/d4sc04105d

a chemically stable and thermally robust network, high crystallinity, high porosity, large surface area and architectural manoeuvrability.[29–33] As a result, MOFs have been designed and developed for various notable applications including heterogeneous catalysis.[34] The metalloligand strategy has also been effectively utilized for the design of diverse architectures including MOFs.[35–38] A metalloligand allows the incorporation of a desired metal ion that may facilitate light absorption in the visible region of the solar spectrum.[39–41] Such a strategy may enable a metalloligand to act as a light harvester in the resultant MOF.[35–41] In contrast, use of an organic ligand(s) in a MOF often lacks this feature.[42] An efficient photocatalyst is typically composed of a photosensitive unit for light harvesting and an active site for a potential catalytic reaction. Metalloligand-based molecular architectures fulfil both these roles well.[35–41] While a metalloligand may act as a light harvester (*i.e.* photosensitizer), the secondary metal ion(s) may function as the catalytic site.[43] Importantly, the electronic structure of the resultant architectures can be manipulated by the selection of (i) the primary metal ion in a metalloligand; (ii) the associated ligand(s) in a metalloligand; and (iii) the secondary metal ion(s).[35–38]

Only a handful examples of metalloligand-based photocatalytic molecular architectures are available in the literature.[44,45] The majority of such examples have utilized photosensitizers that are based on precious metals, such as ruthenium and iridium.[43–45] Furthermore, most of these examples have been utilized either for CO_2 reduction[43] or dye degradation.[43–45] Very rarely have such architectures been utilized for visible-light mediated organic transformations.[46,47] In these cases, such molecular architectures function as semiconductor photocatalysts.[43–45]

Typically, in a semiconductor photocatalysis, a catalyst is activated by light, generating energetic electrons and holes.[15,16,48] Such species can initiate oxidation and reduction reactions to form a series of reactive oxygen species (ROS), such as a superoxide radical ($^{\bullet}O_2^-$), hydroxyl radical ($^{\bullet}OH$) and singlet oxygen ($^1O_2$).[1–3,48] Together with the photogenerated holes (h^+), such ROS can initiate various photocatalytic reactions.[4,9–16,48] In well-documented photocatalytic degradations, photogenerated holes and hydroxyl radicals are the major yet non-selective oxidants with the potential to mineralize organic compounds into simpler products such as CO_2, N_2, H_2O, *etc.*[4,37] Similarly, such potent oxidants can also cause non-selective oxidation of organic substrates; although with significantly lower yield and selectivity of the desired product. Selective oxidation can only be accomplished with milder ROS, such as $^{\bullet}O_2^-$ and $^1O_2$.[4,9] Therefore, the precise control over the generation of ROS is critical for the desired photocatalytic organic transformation. The selective oxidation of alcohols to aldehydes and ketones is an important organic transformation.[49,50] A large number of both natural and synthetic products, pharmaceuticals and drugs contain carbonyl groups, thus emphasizing their significance.[49,50] Sulfoxidation is an equally appealing reaction in organic synthesis, with the desulfurization of fossil fuels and disposal of S-based chemical warfare agents being some of the notable categories.[51,52]

Utilizing semiconductor photocatalysis, there are two pathways for the generation of charge carriers.[1–3,48,53,54] The type-I process relies on electron transfer to generate ROS ($^{\bullet}OH$, $^{\bullet}O_2^-$ and $^1O_2$).[1–5,48] In contrast, the type-II pathway is based on energy transfer from triplet state excitons to molecular oxygen ($^3O_2$) to generate the singlet oxygen ($^1O_2$).[53,54] Besides the lower oxidation potential of a photocatalyst, the formation of triplet state excitons is a prerequisite for the generation of $^1O_2$.[53,54] Such a pathway can be achieved either by incorporating heavy atoms (*e.g.* Bi, I, Se) or by incorporating lanthanide metals that are known for their long triplet state lifetimes.[53–55] Taking these critical points into consideration, in this work, a Co^{3+}-based metalloligand **1**, offering appended arylacrylate groups, has been utilized for the synthesis of lanthanide-based MOFs (Ln-MOFs), **1-Tb** and **1-Eu**. Both structurally characterized Ln-MOFs act as semiconductor photocatalysts and support visible light-driven selective oxidation of alcohols and sulfides. Transient absorption and EPR spectroscopy show electron transfer from the light harvesting metalloligands to the Ln^{3+} ions, generating active Ln^{2+} sites that function as reaction centers. Photoluminescence and phosphorescence studies validate the intersystem crossing. The triplet state excitons facilitate the exclusive generation of singlet oxygen ($^1O_2$), which results in selective oxidation reactions. The photocatalysis results are corroborated by band gap energy calculations and various mechanistic studies, including with a Zn-analogue of **1-Tb** that supports the heavy-metal effect of a lanthanide ion in a Ln-MOF. To the best of our understanding, this work not only provides an excellent substrate scope for catalysis but also comprehensive mechanistic details of the entire photocatalytic process.

Results and discussion

Synthesis and characterization of Ln-MOFs

The two Ln-MOFs, **1-Tb** and **1-Eu**, were synthesized by the reaction of a Co^{3+}-based metalloligand **1** (Fig. S1–S9, ESI†), bearing four appended arylacrylate groups, with a $Ln(OTf)_3$ salt (Ln = Tb, Eu) (Fig. 1). Energy dispersive X-ray (EDX) spectroscopy established the elemental compositions of both Ln-MOFs (Fig. S10, ESI†). X-ray photoelectron spectroscopy (XPS) analysis also showed the presence of Tb^{3+} and Eu^{3+} ions in **1-Tb** and **1-Eu**, respectively, while further confirming the presence of Co^{3+} ions in both MOFs. Additionally, XPS studies revealed that the binding energies of $Co2p_{3/2}$ and $Co2p_{1/2}$ were approximately the same before and after the coordination of the Ln^{3+} ions. Such an observation shows that the oxidation state of the Co ion (+3) remains unaltered in both the metalloligand and Ln-MOFs (Fig. S11–S13, ESI†). Single crystal X-ray diffraction studies revealed that both Ln-MOFs crystallized in a triclinic cell with the $P\bar{1}$ space group (Tables S1–S5, ESI†). The asymmetric unit of the two Ln-MOFs is composed of one metalloligand, one Ln^{3+} ion, one coordinated DMSO and two/three coordinated water molecules (Fig. S14, ESI†).[56] Both MOFs exhibited a very similar structure in which a Ln^{3+} ion is coordinated by two carboxylate groups originating from two different metalloligands, one DMSO and two/three water molecules. In the case of **1-Tb**,

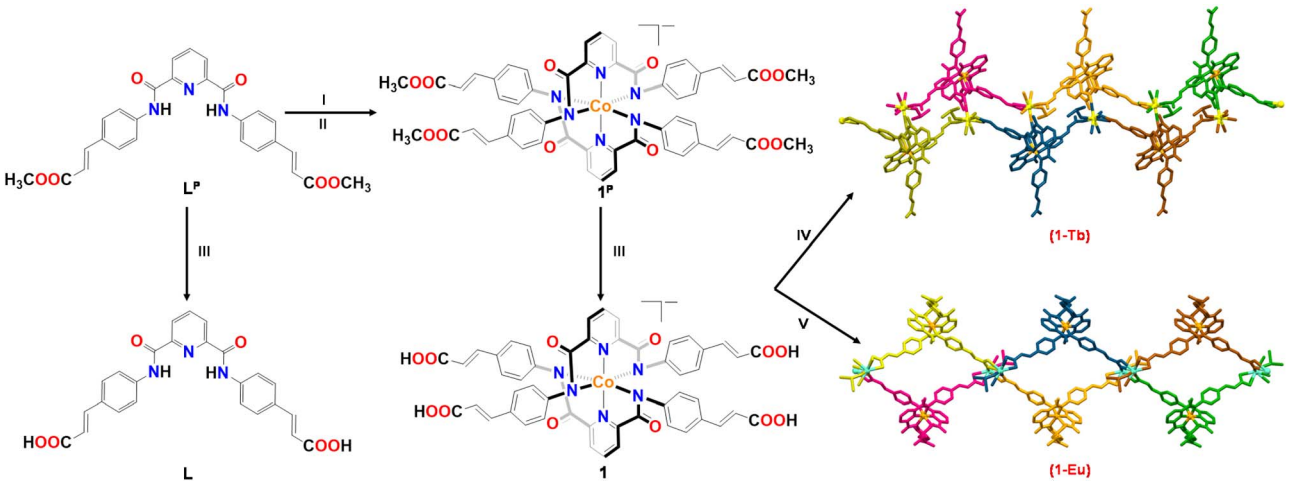

Fig. 1 Synthetic routes and crystal structures of Ln-MOFs **1-Tb** and **1-Eu**. Conditions: I = NaH, DMF; II = Co^{2+} salt, O_2; III = OH^-; IV = Tb^{3+} salt; V = Eu^{3+} salt.

a combination of metalloligands and Tb^{3+} ions generate 1D chains that are connected *via* O_{amide} groups, stemming from another metalloligand, to form a double chain. Such double chains are further joined through assorted H-bonds involving O_{amide} groups of metalloligands and lattice water molecules. The resultant architecture presented large cavities with dimensions of 12.4 × 10.8 $Å^2$. However, in the case of **1-Eu**, two parallel 1D chains are connected together by $O_{carboxylate}$ groups, forming a double-chain structure. The resultant architecture offered large cavities (13.2 × 18.7 $Å^2$). In both Ln-MOFs, while two arylacrylate groups coordinate with the Ln^{3+} ions, the other two remained protonated and uncoordinated.

The presence of large cavities in both Ln-MOFs suggests their porosity, which was substantiated by N_2 sorption experiments. The Ln-MOFs, **1-Tb** and **1-Eu**, exhibited BET surface areas of 42 and 76 $m^2\ g^{-1}$, respectively (Fig. S17, ESI†), consistent with their cavity dimensions.[57] The PXRD patterns of the as-synthesised samples matched very well with the patterns simulated from the single crystal diffraction analyses, indicating phase purity of the bulk samples (Fig. S18, ESI†). The diffuse reflectance spectra (DRS) of **1-Tb** and **1-Eu** exhibited absorptions at *ca.* 620–625 and *ca.* 425–433 nm (Fig. 2a). The Mott–Schottky plots for both Ln-MOFs show positive slopes at two different frequencies (Fig. 2c and d). This is consistent with the behaviour of a typical *n*-type semiconductor.[58] For **1-Tb**, the conduction band position (LUMO), determined from the intersection, was −0.94 V *versus* NHE. The valence band (HOMO) was then calculated to be 1.31 V *versus* NHE. Therefore, the band gap energy of **1-Tb** was found to be 2.25 eV from the Tauc plot using the direct method (Fig. 2b).[59] Similarly, the band gap energy for **1-Eu** was found to be 2.30 eV while the LUMO and HOMO potentials were −1.09 and 1.21 V,

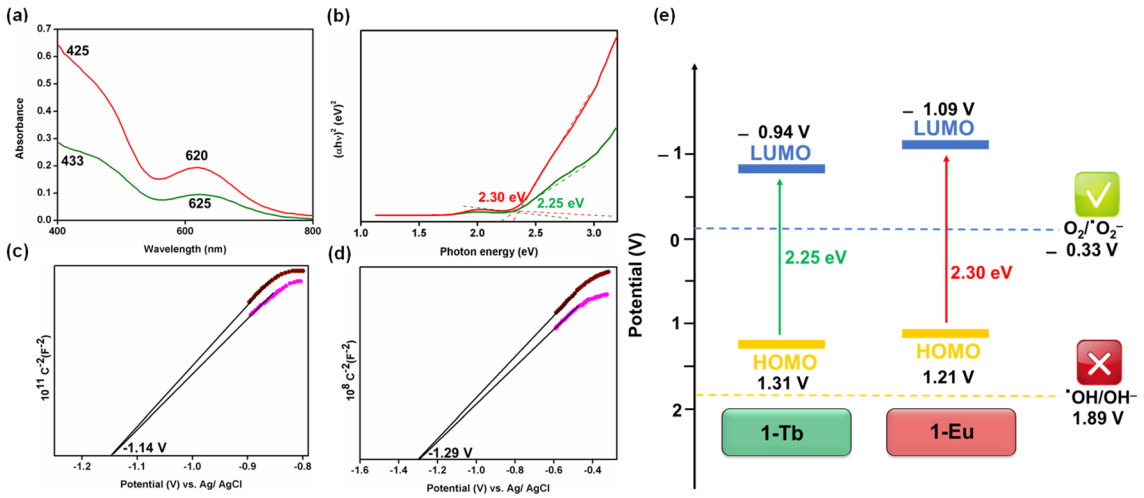

Fig. 2 (a) Diffuse reflectance spectra of **1-Tb** (green trace) and **1-Eu** (red trace). (b) Tauc plots for **1-Tb** (green trace) and **1-Eu** (red trace). Mott–Schottky plots for (c) **1-Tb** and (d) **1-Eu** at two different frequencies; 0.5 kHz (pink spheres) and 1.0 kHz (brown spheres). (e) Energy profiles for **1-Tb** and **1-Eu** depicting HOMO–LUMO positions *versus* NHE.

respectively (Fig. 2b–d). The band gaps for both Ln-MOFs were also fitted using the indirect band gap model as illustrated in Fig. S19, ESI.†,[59] The resulting indirect band gaps for both Ln-MOFs were very close (±0.02) to those calculated using the direct model. These parameters suggest adequate light absorption and electron–hole separation ability of both Ln-MOFs upon visible-light irradiation.[48] Based on these results, energy profiles of both **1-Tb** and **1-Eu** are proposed in Fig. 2e. The band gap positions potentially point toward the generation of superoxide ($^{\bullet}O_2^-$) radicals and not hydroxyl ($^{\bullet}OH$) radicals upon visible light absorption (*vide infra*).[4,9] These results suggest that the present Ln-MOFs could be utilized for visible-light-driven photocatalysis.

Photocatalytic alcohol oxidation

O_2 activation is a critical step in O_2-mediated oxidation reactions.[49,50] To investigate the ability of two Ln-MOFs in O_2 activation, **1-Tb** was employed as a model catalyst for the oxidation of benzyl alcohol. **1-Tb** efficiently promoted the oxidation of benzyl alcohol to benzaldehyde under visible light irradiation in the presence of air in water at 20(±1) °C. Notably, benzoic acid was not detected, even when the reaction was allowed to run for a longer duration. This reaction provided good evidence for the selective photo-oxidative behaviour of Ln-MOFs.

Subsequently, the reaction conditions were optimized taking benzyl alcohol as a model substrate while catalytic reactions were performed in water under visible light irradiation (Table 1). **1-Tb** acted as an efficient and selective photocatalyst by only producing benzaldehyde (**1a**; Scheme 1, *vide infra*) with >99% isolated yield within 15 min (entry 1, Table 1). This reaction provided a turnover number (TON) of 279 and a turnover frequency (TOF) of 19 min^{-1}. The Eu-analogue, **1-Eu**, also resulted in the quantitative oxidation of benzyl alcohol (entry 2). The photocatalytic nature of the oxidation reaction was established by a series of control experiments (Table 1). Reaction without a photocatalyst (entry 3) or in the absence of visible light under otherwise identical conditions (entry 4) did not produce any benzaldehyde. These reactions confirm the photocatalytic nature of the transformation.[37] To rule out the possibility of a thermal reaction, catalysis was attempted at elevated temperature (60 °C) but without any light source. Such a reaction only resulted in a negligible amount of a product (entry 5), confirming that the oxidation of benzyl alcohol is exclusively driven by the visible light.[49] The photocatalytic reaction was also performed using sunlight as the irradiation source and a nearly quantitative yield was obtained (entry 6). This illustrates that sunlight can be conveniently used for the oxidation reaction. As expected, no product was produced in the absence of O_2 (entry 7), while the presence of air reduced the benzaldehyde yield (entry 8). Importantly, metalloligand **1** did not promote the photocatalytic oxidation of benzyl alcohol (entry 9; *vide infra*). The **1-Tb** catalyzed oxidation of benzyl alcohol was used to investigate the reaction kinetics.[16] A plot of $\ln(C_t/C_o)$ *versus* time revealed first-order kinetics with a rate constant of 9.27×10^{-2} min^{-1} (Fig. 3a and S20, ESI†).[37] A high-rate constant confirms a fast photocatalytic reaction. It can be noted that rate constants have rarely been calculated for photocatalytic reactions;[15,16] while rate constants using external oxidants (*e.g.* H_2O_2) are inferior to that of the present Ln-MOFs.[4,5,15,16]

To investigate the nature of the ROS involved in the oxidation of benzyl alcohol, different scavengers were used. The use of NaN_3, isopropyl alcohol and *para*-benzoquinone are known to specifically inhibit the generation of $^1O_2$, $^{\bullet}OH$ and $^{\bullet}O_2^-$, respectively.[37,60] The oxidation of benzyl alcohol was significantly suppressed by the use of NaN_3 (<12% isolated yield, 88% inhibition, entry 10). Meanwhile, the presence of isopropyl alcohol ($^{\bullet}OH$ scavenger) did not affect the oxidation of benzyl alcohol (entry 11), and the use of *para*-benzoquinone ($^{\bullet}O_2^-$ scavenger) only partially inhibited its oxidation (entry 12). These results suggest that $^1O_2$ is the primary ROS involved in the photocatalytic oxidation of benzyl alcohol (*vide infra*).

To further confirm the generation of $^1O_2$ by light irradiation, a few $^1O_2$ selective probes, such as 9,10-dimethylanthracene (DMA) and 1,5-dihydroxynapthalene (DHN) were utilized.[49,61] The intense fluorescence of DMA, at 427 nm, was significantly quenched in the presence of **1-Tb** under visible light irradiation. This indicates that DMA was oxidized by $^1O_2$ to endoperoxide, DMA-O_2 (Fig. 3b).[49] Likewise, the absorbance of DHN at 301 nm was decreased upon exposure to visible light in the presence of **1-Tb**. Furthermore, a new band was generated at 420 nm due to the photooxidative depletion of DHN to form 5-hydroxy-1,4-napthalenedione (juglone) on reaction with $^1O_2$ (Fig. 3c).[61] These results corroborate the generation of $^1O_2$ as the predominant ROS. The kinetics were studied by monitoring the change in the absorption peak of juglone at 420 nm, and the rate constant was calculated to be 0.0542 min^{-1} (Fig. S21, ESI†). The calculated rate constant is higher than that observed for other common photocatalysts reported in the literature (Table

Table 1 Control and optimization experiments for the photocatalytic oxidation of benzyl alcohol

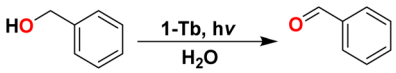

Entry[a]	Reaction parameters	Isolated yield (%)
1	**1-Tb**, O_2, 15 min	>99 TON = 279 TOF = 19 min^{-1}
2	**1-Eu**, O_2, 20 min	>99
3	No catalyst, O_2, 60 min	NR
4	**1-Tb**, O_2, no light, 60 min	NR
5	**1-Tb**, O_2, 60 °C, no light, 30 min	6
6	**1-Tb**, O_2, sunlight, 30 min	98
7	**1-Tb**, N_2, 30 min	NR
8	**1-Tb**, air, 15 min	68
9	**1**, O_2, 30 min	NR
10	**1-Tb**, O_2, NaN_3, 15 min	12
11	**1-Tb**, O_2, isopropyl alcohol, 15 min	98
12	**1-Tb**, O_2, *p*-benzoquinone, 15 min	84

[a] Reaction conditions: benzyl alcohol (0.92 mmol), photocatalyst (1 mol%), water (2 mL), temperature (25 °C). TON = $mol_{benzaldehyde} \times mol_{1\text{-}Tb}^{-1}$; TOF = TON/15 min. NR = No reaction.

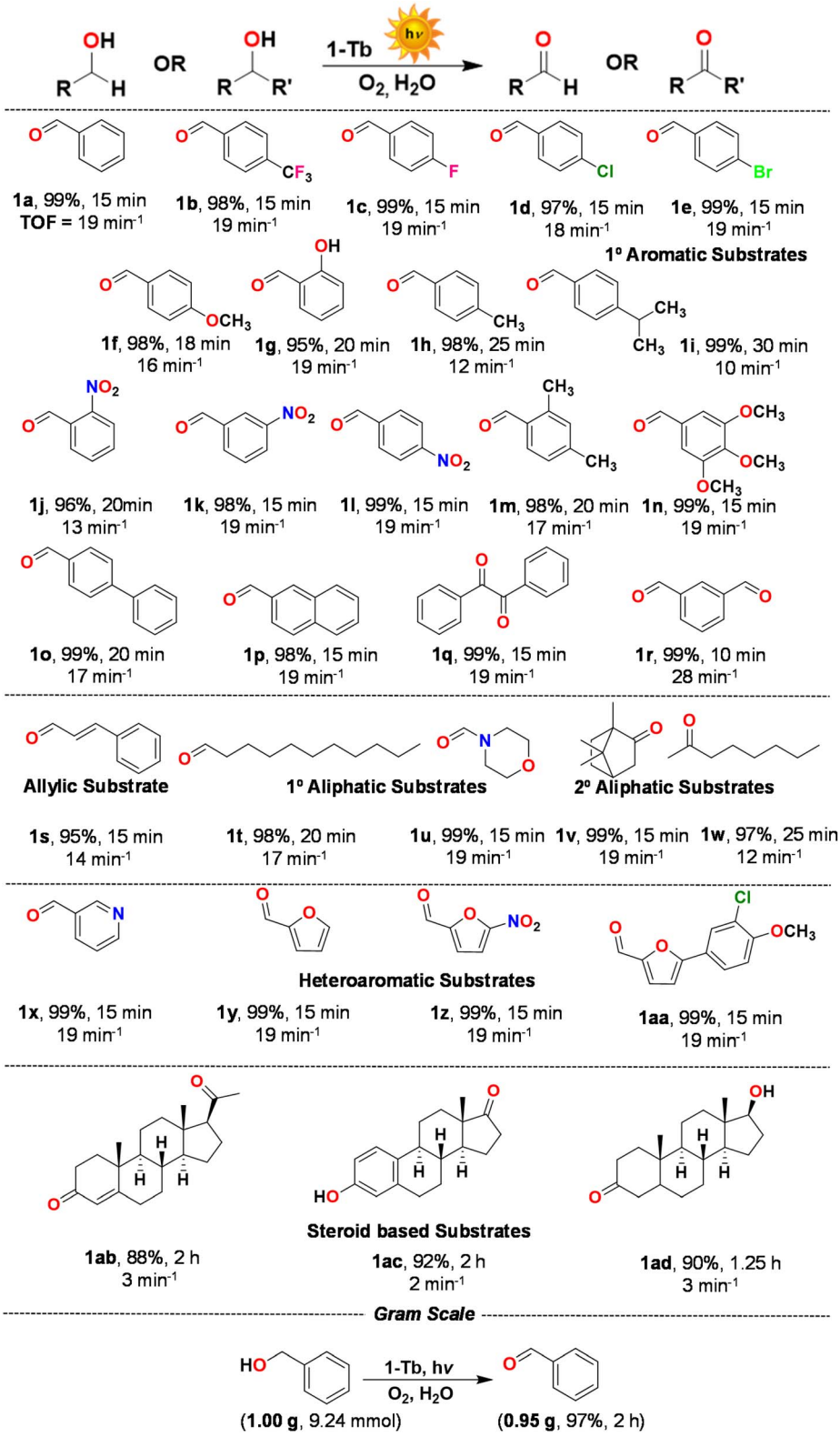

Scheme 1 Substrate scope for the photocatalytic oxidation of assorted alcohols and a scale-up reaction. Reaction conditions: substrate (0.92 mmol), **1-Tb** (1 mol%), H_2O (2 mL), temperature (25 °C). All yields are for the isolated products. The characterization data and the corresponding spectra for the representative products are presented in Fig. S22–S84, ESI.†

S6, ESI†).[61] This indicates superior capacity of the present Ln-MOFs for generating $^1O_2$. Finally, a very high concentration of $^1O_2$, based on **1-Tb** was calculated to be *ca.* 84 μM.

Since radical scavenger experiments suggest that species other than $^1O_2$ could also be involved in substrate oxidation, we investigated whether other ROS ($^{\bullet}OH$ and $^{\bullet}O_2^-$) are also formed

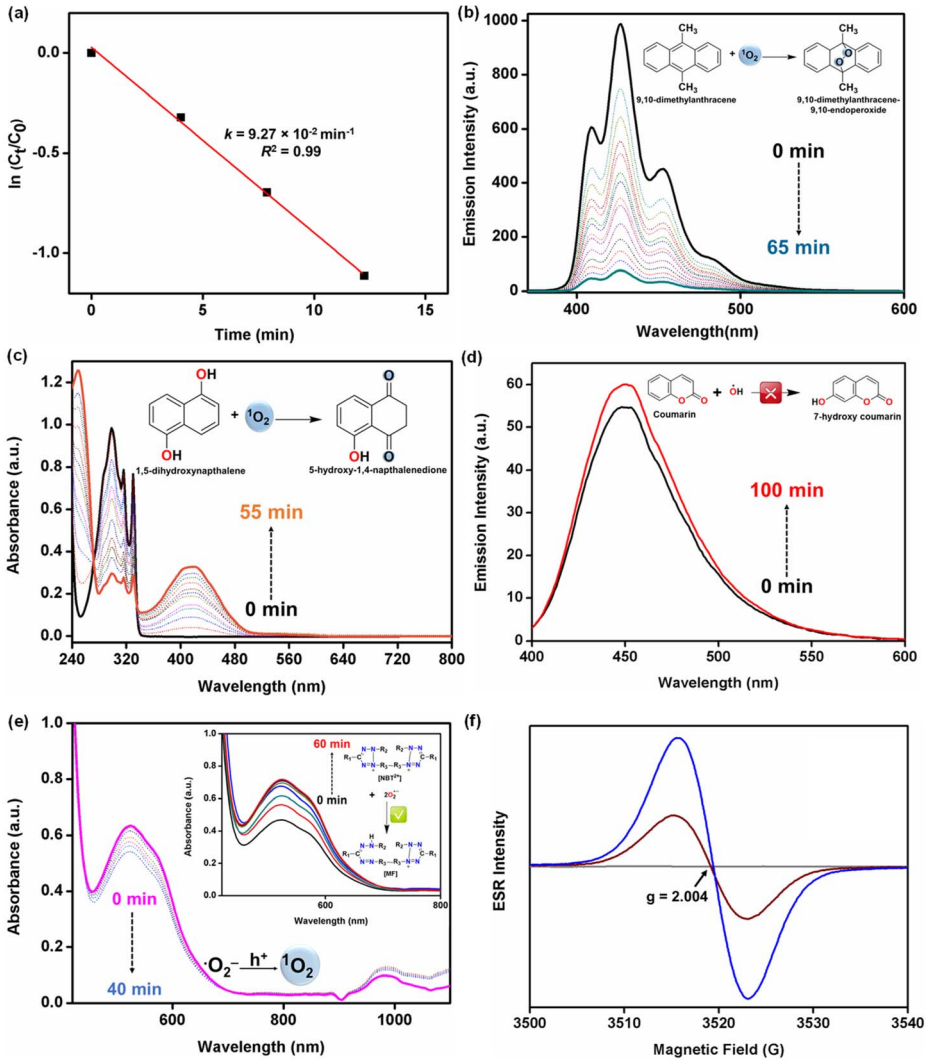

Fig. 3 (a) Plot of $\ln(C_t/C_o)$ *vs.* time for the photo-oxidation of benzyl alcohol. (b) Emission spectrum for the quenching of 9,10-dimethylanthracene under visible-light irradiation at different times (0–65 min at an interval of 5 min). (Inset) A chemical reaction forming 9,10-dimethylanthracene-9,10-endoperoxide. (c) Absorption spectrum for the generation of 5-hydroxy-1,4-napthalenedione under visible-light irradiation at different times (0–55 min at an interval of 5 min). (Inset) A chemical reaction of 1,5-dihydroxynapthalene and $^1O_2$. (d) Emission spectrum for the proposed generation of 7-hydroxycoumarin under visible light irradiation at different times (0–100 min). (Inset) A chemical reaction between coumarin and the $^{\bullet}OH$ radical. (e) Absorption spectrum for the decay of NBT-MF under visible-light irradiation at different times (0–40 min at an interval of 5 min) and a reaction between $^{\bullet}O_2^-$ and holes to form $^1O_2$. (Inset) Absorption spectrum for the formation of NBT-MF from NBT under visible-light irradiation at different times (0–60 min at an interval of 5 min) and a chemical reaction between NBT and $^{\bullet}O_2^-$ to form MF. (f) X-band EPR spectra under dark conditions (grey trace) and visible-light irradiation at different times (brown and blue traces). All studies are in the presence of **1-Tb**.

in good quantities. Coumarin is particularly helpful for identifying $^{\bullet}OH$ radicals as it forms 7-hydroxycoumarin, which is emission active.[37,62] However, insignificant emission enhancement was noted, suggesting that the hydroxyl radicals are not the primary oxidant in the present case (Fig. 3d). This is further supported by the fact that the HOMO potentials for both Ln-MOFs are not sufficiently positive (E_{VB}: **1-Tb** = 1.31 V, **1-Eu** = 1.21 V) to support the generation of a highly active yet non-selective oxidant, $^{\bullet}OH$ [$E(^{\bullet}OH/OH^-) = 1.89$ V *vs.* NHE] (Fig. 2e).[9]

The scavenger nitro-blue tetrazolium (NBT) is exclusively selective for $^{\bullet}O_2^-$.[37,62] During the course of reaction for 60 min in an O_2 saturated environment, a prominent absorption band was observed at 530 nm due to the formation of NBT-formazan. A spectral titration allowed the calculation of the concentration of $^{\bullet}O_2^-$ radicals, which was found to be *ca* 6 μM (Fig. 3e, inset). Importantly, however, the concentration of NBT-formazan species decreased rapidly. This suggests two possibilities; either consumption of $^{\bullet}O_2^-$ radicals or conversion of $^{\bullet}O_2^-$ radicals into some other species (Fig. 3e). The consumption of $^{\bullet}O_2^-$ radicals is ruled out in the absence of any suitable reactant. However, $^{\bullet}O_2^-$ radicals are known to react with holes (h^+) to form $^1O_2$.[4,62] In fact, the generation of $^1O_2$ is certainly conceivable in the present case as per the energy profile (*cf.* Fig. 2e).

In essence, the proposed mechanism for the oxidation of benzyl alcohol is consistent with the activation of O_2 to primarily produce $^1O_2$ (*ca.* 84 μM) along with the limited generation of $^{\bullet}O_2^-$ (*ca.* 6 μM) under visible light irradiation. The band gap energies for both Ln-MOFs (**1-Tb**: 2.25 eV, **1-Eu**: 2.30 eV) are ideal, favouring a facile generation of the mild oxidant, $^1O_2$, while inhibiting the generation of a stronger but non-selective oxidant, $^{\bullet}OH$. To further provide evidence for the generation of ROS, electron paramagnetic resonance (EPR) spectra were recorded under visible light irradiation. Upon visible light irradiation, a sharp EPR spectral signal was detected at $g = 2.004$ ($A_H = 4$ G), supporting a radical-based-intermediate ($^1O_2$/$^{\bullet}O_2^-$) (Fig. 3f).[62]

Of the two MOFs, **1-Tb** catalyzed the oxidation of benzyl alcohol in a shorter span of time, therefore acting as a better photocatalyst (entries 1 and 2, Table 1). Therefore, **1-Tb** was used to explore the substrate scope by attempting the oxidation of assorted alcohols. Various mono- (**1b–1l**), di- (**1m**) and even tri-substituted (**1n**) benzyl alcohols were quantitatively oxidized with exclusive selectivity for an aldehyde (Scheme 1). The type and nature of a substituent(s) on an aromatic ring did not play a significant role in the reaction outcome, since all corresponding products were obtained in nearly quantitative yields. These results strongly suggest a radical mediated catalytic pathway. However, substrates bearing electron-donating groups required a slightly longer time for the completion of a reaction when compared to the substrates with electron-withdrawing groups.[49] Similarly, *o*-substituted benzyl alcohol (**1i**) needed a longer duration than that of *m*- and *p*-isomers (**1j** and **1k**), most probably due to the steric hindrance.[63]

Substrates bearing multiple aromatic rings such as 4-biphenylmethanol and 2-napthylmethanol were successfully oxidized providing the corresponding aromatic aldehydes in excellent yields (**1o**, **1p**). Likewise, dihydroxy substrates, such as hydrobenzoin and 1,3-phenylenedimethanol, were also efficiently oxidized to their corresponding carbonyl compounds in quantitative yields (**1q**, **1r**). On photocatalytic oxidation of cinnamyl alcohol (allylic alcohol), the desired α,β-unsaturated aldehyde was obtained in 96% yield (**1s**), thus highlighting the chemoselectivity.[63] Notably, aliphatic alcohols, such as undecane-1-ol and morpholinomethanol, also afforded the desired aldehydes (**1t**, **1u**) in high yield and exclusive selectivity. These examples justify the present Ln-MOFs as effective photocatalysts for the oxidation of aliphatic alcohols. It is significant that the selective oxidation of aliphatic alcohols has seldom been reported as controlling their over-oxidation is particularly challenging.[64]

In order to further expand the substrate scope, the oxidation of secondary aliphatic alcohols was attempted. For example, both 1,7,7-trimethylbicyclo[2.2.1]heptan-2-yl)methanol and octan-2-ol yielded the corresponding ketones in high yields (**1v**, **1w**). The oxidation of heteroaromatic alcohols such as 3-pyridinemethanol, furan-2-ylmethanol, 5-nitrofuran-2-ylmethanol and (5-(3-chloro-4-methoxyphenyl)-furan-2-yl)methanol also afforded the expected aldehydes in excellent yields (**1x-1aa**). Collectively, a broad range of both primary and secondary alcohols were exclusively oxidized to their corresponding aldehydes and ketones. In order to illustrate the oxidation of challenging substrates, a few steroid-based aliphatic alcohols such as 20α-hydroxysteroid progesterone, 17β-estradiol and 3α/β-androstanediol were employed.[63] Notably, in all three cases, the corresponding products were obtained in excellent yields (**1ab-1ad**). Finally, considering a straightforward process, a gram scale reaction was performed. With 1 g of benzyl alcohol, the reaction took longer (2 h), but an exclusive and quantitative amount of benzaldehyde was obtained (0.95 g; 97%), thus demonstrating a remarkable catalytic performance of Ln-MOFs (Scheme 1).

Although a few reports in the literature mention the use of nanoparticles and composite-materials for the selective oxidation of alcohols,[49] very few MOFs are known to be successful for this reaction.[55,65] Importantly, the photocatalytic efficiency of the present Ln-MOFs for alcohol oxidation is far superior to that of most of the previously reported MOFs and composite materials (Table S7, ESI†). More importantly, the reported examples lack a detailed substrate scope and mechanistic investigations (*vide infra*).[49,55,56,65]

In the present catalytic system, the oxidation of an alcohol is predominantly associated with the action of $^1O_2$, as suggested by the scavenger studies. Based on these findings, a plausible mechanism is proposed in Fig. S85, ESI.† Upon visible light irradiation, a Ln-MOF gets photoexcited followed by the separation of an electron and a hole. The photo-electron activates O_2 to $^1O_2$ which oxidizes benzyl alcohol to a benzyloxy radical (I) that rearranges to a carbon-centred radical (II).[65] The species II subsequently reacts with $^{\bullet}OOH$ to form a peroxy hemiacetal (III) which decomposes to give benzaldehyde as the final product and hydrogen peroxide (H_2O_2) as a by-product. Importantly, the by-product H_2O_2 was confirmed using UV-Vis spectral monitoring of triiodide ions using an aqueous solution of KI (Fig. S86, ESI†).[66] More importantly, H_2O_2 was quantitively estimated by titrating it against a $KMnO_4$ solution that provided its concentration as 2.68 μM.[67] Considering that H_2O_2 could also be a potential oxidant, a control experiment involving gallic acid as an H_2O_2 scavenger was carried out.[68] Notably, however, the quantitative oxidation of benzyl alcohol to benzaldehyde was noted in the presence of gallic acid. This confirms that the photocatalytic oxidation of benzyl alcohol does not depend on *in situ* formed H_2O_2.

Reusability experiments

To establish the recyclability and long-term stability of Ln-MOFs, the photo-oxidation of benzyl alcohol, as a model substrate, was carried out using **1-Tb**, as a representative catalyst. After the reaction, **1-Tb** was recovered using a centrifuge, washed three times with water, and reused for the photooxidation of a fresh batch of benzyl alcohol. Notably, **1-Tb**, as a catalyst, was reused for fifteen consecutive cycles. While there was negligible change in product yield during the first ten cycles, a slight decrease (2–4%) was observed between the 12th and 15th cycles (Fig. S87, ESI†). However, complete selectivity was maintained throughout all 15 cycles. Furthermore, both the FTIR spectra and PXRD patterns of the recovered catalyst did

not exhibit any significant change compared to the as-synthesized **1-Tb**, indicating its stability and recyclability as a heterogeneous photocatalyst (Fig. S88 and S89, ESI†). Additionally, both SEM and optical images of the recovered sample did not show any obvious change compared to those of as-synthesized **1-Tb** indicating preservation of its surface morphology (Fig. S90, ESI†). These results confirm the remarkable stability and recyclability of Ln-MOF photocatalysts that can serve as potential candidates for commercial processes.

Photocatalytic sulfide oxidation

The outstanding photocatalytic oxidation of assorted alcohols inspired us to extend the photocatalysis to other substrates such as sulfides. Oxidation of sulfides is significant in many fields including organics and pharmaceuticals, petroleum products and environmental remediation.[51,52] Initially, photocatalytic oxidation of thioanisole was chosen as a model reaction to optimize the reaction conditions. Thioanisole was quantitatively oxidized to methylphenyl sulfoxide (**2a**; Scheme 2) with 100% selectivity, 242 TON and 16 min^{-1} TOF under visible light irradiation in MeOH in the presence of **1-Tb** as a catalyst. The type and nature of the solvent had a significant impact on the catalytic outcome (Table S8, ESI†). In the presence of an aprotic solvent (*e.g.* DMF, MeCN, THF), the isolated yield was low (60–80%). A polar protic solvent (such as H_2O) resulted in a higher product yield (84%); however, quantitative oxidation was noted in MeOH and EtOH.[51,52] Importantly, in all cases, irrespective of the reaction duration and/or solvent used, only sulfoxide was obtained without any trace of undesired sulphone.

1-Tb exhibited a good substrate scope with very high yield for most of the sulfides. Photooxidation of diphenylsulfide, dibenzylsulfide and their substituted analogues bearing both electron-withdrawing and electron-donating groups produced the corresponding sulfoxides in excellent yields (**2b–2f**). A nearly quantitative yield was obtained for the photooxidation of tetrahydrothiophene (**2g**), a cyclic sulfide. Importantly, several aliphatic sulfides (n = 4, 8 and 10) also yielded the respective sulfoxides (**2h–2j**) in high yields. More importantly, both the yield and the selectivity were not compromised for any such substrate. Subsequently, sulfoxidation of thioanisole was carried out on a gram scale that exclusively yielded 1.02 g of methylphenyl sulfoxide in 92% isolated yield (Scheme 2). The same reaction was used to monitor the rate of sulfoxidation. The formation of methylphenyl sulfoxide was found to follow first-order kinetics with a rate constant of 0.0562 min^{-1} (Fig. 4a and S114, ESI†). The photooxidation efficiency and selectivity of **1-Tb** towards different sulfides either matched or exceeded the reported examples.[51,54,60] It is worth mentioning that several such literature examples suffered from the formation of undesirable sulfone (Table S9, ESI†).[60]

Finally, **1-Tb** was used for the detoxification of a mustard gas simulant, 2-chloroethyl-ethyl-sulfide (CEES).[51,52] Only 1 mol% of **1-Tb** exclusively oxidized CEES to non-toxic 2-chloroethyl-ethyl-

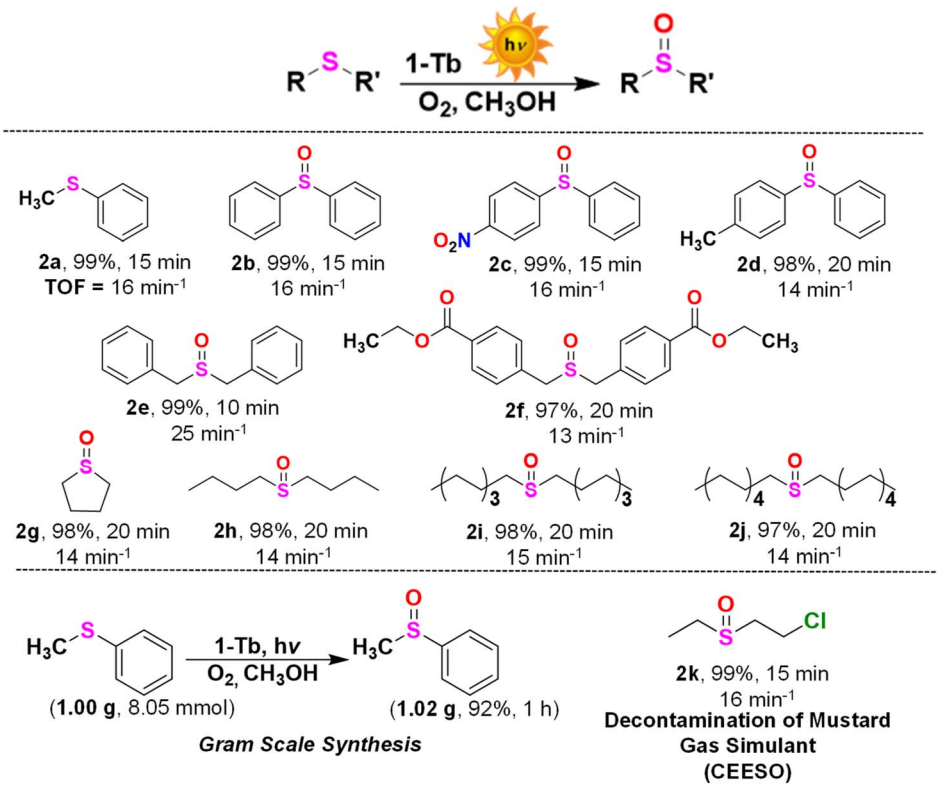

Scheme 2 Substrate scope for the photocatalytic oxidation of assorted sulfides, a scale-up reaction and photocatalytic oxidation of 2-chloroethyl-ethyl-sulfide (CEES). Reaction conditions: substrate (0.80 mmol), **1-Tb** (1 mol%), MeOH (2 mL), temperature (25 °C). All yields are for the isolated products. The characterization data and the corresponding spectra for representative products are presented in Fig. S91–S113, ESI.†

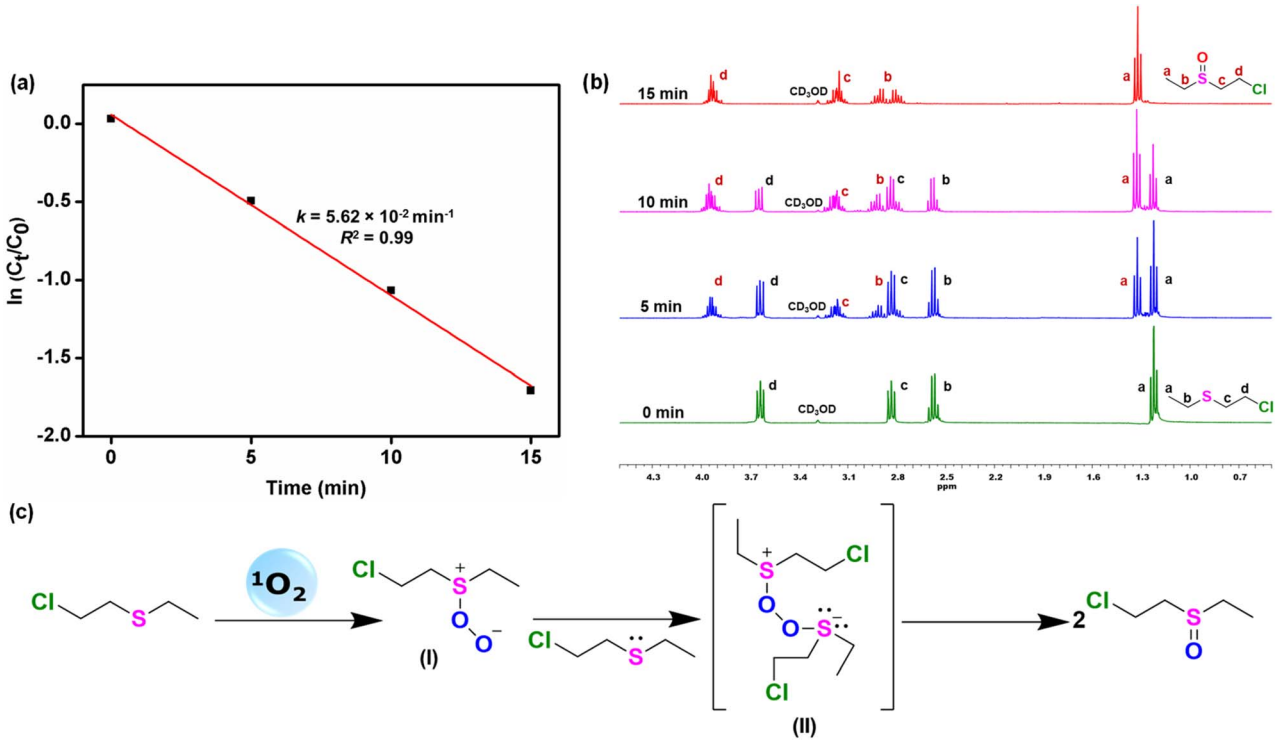

Fig. 4 (a) Plot of $\ln(C_t/C_o)$ *versus* time representing first-order kinetics for the photo-oxidation of thioanisole in the presence of **1-Tb** as a photocatalyst. (b) Progress of the sulfoxidation reaction of CEES monitored by time-dependent ^{1}H NMR spectra. (c) Proposed reaction mechanism for the selective oxidation of CEES using $^1O_2$.

sulfoxide (CEESO, **2k**). The selectivity for this photooxidation was evaluated by proton NMR spectral experiment (Fig. 4b). New signals were identified at 1.37, 2.85, 2.95, 3.19, and 3.98 ppm, which were consistent with the formation of CEESO replacing the characteristic CEES peaks at 1.27, 2.61, 2.88, and 3.67 ppm. The reaction was complete within 15 min and only sulfoxide was formed as the exclusive product. Even after 24 h of the initial photo-irradiation, no sulfone could be detected. Similar to the selective oxidation of alcohols, only a few materials are known for the oxidation of sulfides.[51,52] In comparison to the reported examples, the present Ln-MOF photocatalysts offered a considerable improvement in the photocatalytic activity, selectivity and substrate scope.[61,65]

Based on radical scavenger experiments, $^1O_2$ is the key ROS involved in the oxidation reactions. Accordingly, a mechanistic pathway for the photooxidation of CEES is proposed (Fig. 4c). Upon nucleophilic addition of the thioether substrate to the electrophilic $^1O_2$, a weakly bound persulfoxide intermediate I is formed. Intermediate I undergoes quenching in a polar aprotic solvent while it is stabilized in a protic solvent by H-bonding, thus substantially enhancing the effectiveness of the photooxidation in polar protic solvents.[51,52] Control experiments also supported this assertion (Table S6, ESI†). As a consequence of the nucleophilic reaction between intermediate I and another molecule of CEES, an unstable anionic hypervalent intermediate II is formed.[51,52] Such an unstable intermediate breaks down to give two molecules of sulfoxide, CEESO. Therefore, each molecule of singlet oxygen has the ability to produce two equivalents of sulfoxide, justifying a fast and efficient oxidation of CEES to CEESO.

Mechanistic insights

The Ln-based photocatalysts are primarily composed of two key components, the Co^{3+}-based metalloligands (**1**) and the secondary Ln^{3+} ions. Despite the fact that metalloligand **1** absorbs in the visible region of the spectrum, it was unable to drive a photocatalytic oxidation reaction (entry 9; Table 1). Therefore, it became essential to identify the structural constituent(s) that is actually responsible for the generation of singlet oxygen and subsequent photooxidation. For this purpose, ultrafast transient absorption spectroscopy (TAS) measurements were performed for ligand **L** (the organo-analogue of **1**), metalloligand **1** and Ln-MOF **1-Tb**, with all samples being excited at 375 nm and probed using white light continuum over a wavelength range of 400–700 nm. The transient absorption (TA) spectra as a function of different delay times are shown in Fig. 5a–c along with the associated kinetics (Fig. 5d–f) and global fitting analyses (Fig. S115, ESI†). All samples show distinct and well-developed excited state absorption (ESA) spectra with λ_{max}^{ESA} varying depending on the sample identity.[69] For example, a Co^{3+}-based metalloligand **1** shows a prominent red shift at 590 nm compared to ligand **L** (565 nm). Bi-exponential global fitting analyses of both **L** and **1** show a faster component (~200 fs for **L** and ~600 fs for **1**) and a relatively slower component (~33 ps for **L** and ~64 ps for **1**) (Fig. S115a and b, ESI†). We attribute the faster component to

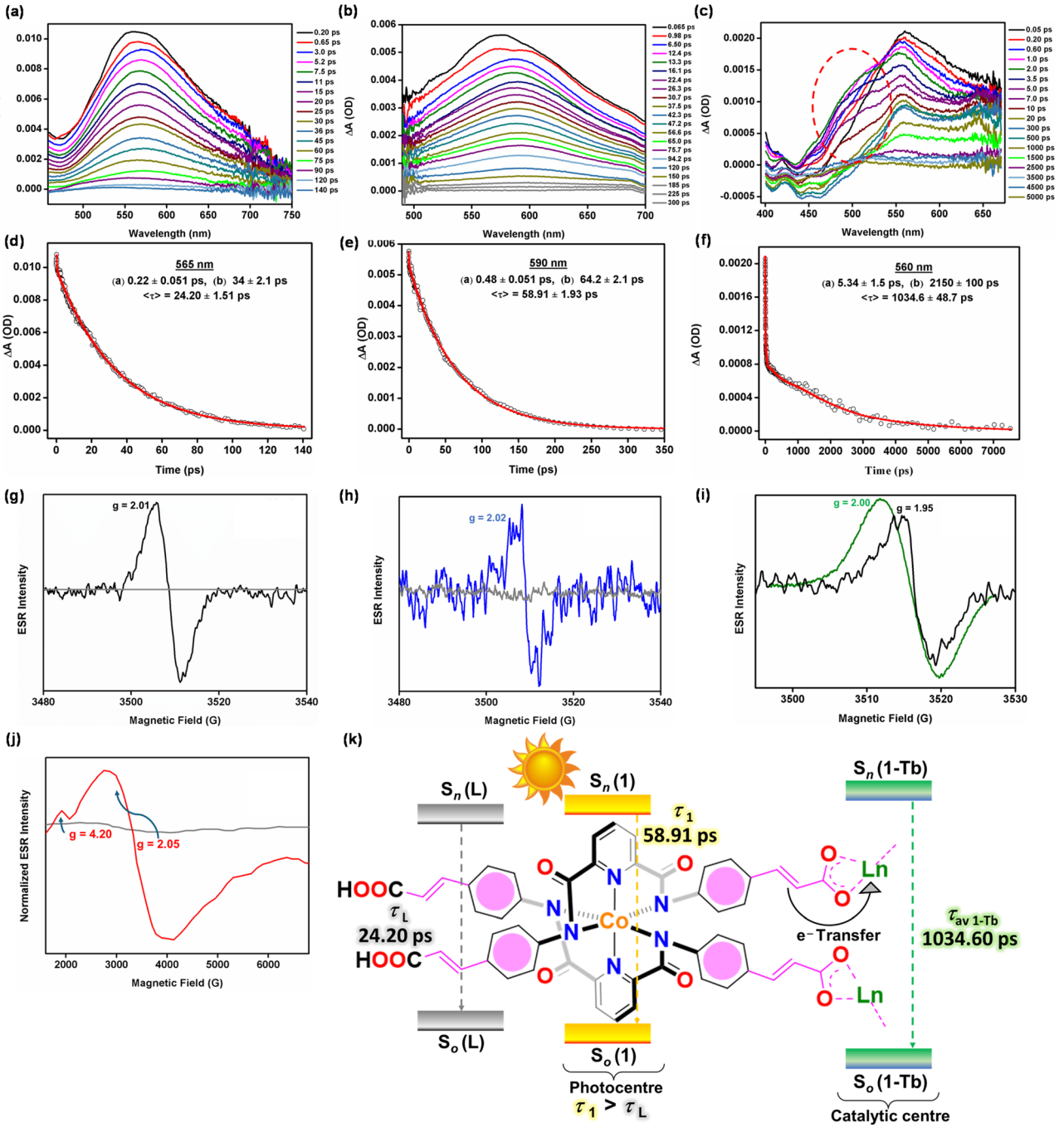

Fig. 5 Ultrafast transient absorption spectra for (a) **L**, (b) **1** and (c) **1-Tb** (λ_{pump} = 375 nm) and the corresponding decay kinetics (probed at the maximum of the excited-state absorption spectra) of (d) **L** at 565 nm, (e) **1** at 590 nm, and (f) **1-Tb** at 560 nm. *In situ* EPR spectra for (g) **1** where the grey and black traces represent spectra under dark conditions and under visible-light irradiation, respectively; (h) **L** where the grey and blue traces represent spectra under dark conditions and under visible-light irradiation, respectively; (i) **1-Tb** where the green and black traces represent spectra under dark conditions and under visible-light irradiation, respectively; and (j) **1-Eu** where the grey and red traces represent spectra under dark conditions and under visible-light irradiation, respectively. (k) A schematic representation of comprehensive data analysis of ultrafast transient absorption spectroscopy for **L**, **1** and **1-Tb**.

intra-molecular vibrational relaxation (IVR) and internal conversion (IC) while the slower one corresponds to the decay of the excited state singlet to the ground state of a sample. Superimposition of the decays shows a longer average decay time ($\tau_{av(1)}$ = 58.91 ps) for **1** when compared to **L** ($\tau_{av(L)}$ = 24.20 ps) (Fig. S116, ESI†). This suggests greater electron delocalization in a metalloligand arising from the mixing of ligand-π and cobalt-d orbitals and hence facilitation of its role as a photosensitizer in the resultant architecture.[44,45]

For **1-Tb**, along with a 5 nm blue shift of λ_{max}^{ESA} to 560 nm, unlike the TA spectra of both **L** and **1**, the growth of a shoulder in the ESA is seen to develop at around 200 fs (with the

wavelength maximum of the shoulder being at around 470 nm), and this develops into a negative ΔA peak at around 450 nm at 20 ps (Fig. 5c). Moreover, the global bi-exponentially fitted kinetic profile also reveals an interesting probe wavelength dependency (Fig. S115, ESI†). For the probe wavelength range of 450–535 nm, an increase in the signal (with negative amplitude) of ~2 ps is observed alongside a slower component of ~6 ps (IC; τ_D = time scale of intra-molecular vibrational relaxation; Fig. S115c, ESI†). Beyond 540 nm, this growth component is replaced by a decay component with a long lifetime of 2075 ps (Fig. S115c, ESI†). We propose that this increase in signal, which implies the development of a photoproduct, corresponds to the generation of a Tb^{2+} state after a facile electron transfer from the metalloligand to the Tb^{3+} ion on a timescale of ~2 ps (τ_{ET} = time scale of electron transfer).

To gain further insights into the photo-induced electron transfer, EPR spectral experiments were carried out.[13] The EPR spectrum of **1**, under dark conditions and a N_2 environment, did not exhibit any signal owing to the presence of a Co^{3+} ion (d^6, $S = 0$). Upon visible-light irradiation, a distinct signal at $g =$ 2.01 (Δ_H = 6 G) was observed (Fig. 5g). When the light was turned off, the signal immediately disappeared, thus confirming visible-light-induced radical formation. A relatively small value of g suggests that electron transfer during the photo-induced process did not occur from the primary metal ion, Co^{3+}, but rather from the organic ligand of metalloligand **1**. To substantiate this, **L** was also subjected to the EPR spectral investigation under visible light-irradiation. The EPR spectrum of photo-induced **L** (g = 2.02; Δ_H = 4 G) was very weak but similar to the one observed for **1** (Fig. 5h). This confirms that photo-induced electron transfer occurs from the organic ligand of metalloligand **1**. Importantly, the EPR spectrum of **1-Tb**, under an inert atmosphere, showed a broad signal at $g = 2.00$ (Δ_H = 8 G), corresponding to a Tb^{3+} ion.[70] Upon visible light irradiation, a rather complex EPR spectrum was obtained (Fig. 5i), in which a sharper signal is attributed to the paramagnetic Tb^{2+} ion (g = 1.95; Δ_H = 4 G). These results unambiguously validate electron transfer from a metalloligand to a Tb^{3+} ion thus generating a Tb^{2+} site. To further support this, EPR spectra were also measured for **1-Eu**. In the absence of visible light, no signal was detected as both Co^{3+} and Eu^{3+} ions are EPR inactive.[39] However, upon visible light irradiation, signals at $g = 2.05$ (Δ_H = 4 G) and $g = 4.20$ (Δ_H = 9 G) appeared (Fig. 5j). Such an EPR spectrum is attributed to a paramagnetic Eu^{2+} species, generated as a result of electron transfer from a metalloligand to an Eu^{3+} ion.[39] Subsequently, an excited Ln^{2+} ion transfers its energy to the triplet oxygen ($^3O_2$) to generate singlet oxygen ($^1O_2$), which is responsible for the photooxidation reactions. Finally, electron transfer from a Ln^{2+} ion to a metalloligand completes the catalytic cycle. In summary, Fig. 5k illustrates a schematic representation of ultrafast TAS results for **L**, **1** and **1-Tb**.

To further support electron transfer, the photoluminescence (PL) of metalloligand **1** and Ln-MOF **1-Tb** were analysed. Both **1** and **1-Tb** displayed strong absorption bands at 400–600 and 400–650 nm, respectively (inset of Fig. 6a and 2a). While an intense absorption band at 400–500 nm corresponded to a Co^{3+}-centered metal-to-ligand charge transfer (MLCT) transition, a relatively weak absorption band, at higher wavelength, is ascribed to the d–d transition of the primary Co^{3+} ion. Notably, the absorption spectrum of **1-Tb** closely matches that of metalloligand **1**, thus suggesting that the coordination of the secondary metal ions (Tb^{3+}) has not significantly perturbed the electronic environment of the Co^{3+} ion in **1**.[24] It was thus assumed that coordination of a Tb^{3+} ion to a metalloligand should not significantly affect its PL properties. However, the PL intensity of **1-Tb** (at 452 nm) was significantly quenched when compared to the metalloligand **1** (Fig. 6a). A much lower emission intensity for **1-Tb** suggests a reduced population of the singlet excitons since fluorescence results from the radiative decay of the singlet excitons.[55] Notably, typical Tb^{3+}-based f–f emissions were also not observed in the PL spectrum of **1-Tb**. This further confirms electron transfer from a metalloligand to a Tb^{3+} ion in the resultant Ln-MOF.[71,72] Additionally, it suggests that the recombination rate of photo-generated charge carriers is higher in metalloligand **1** than in the Ln-coordinated-metalloligand (*i.e.* **1-Tb**).[71] This is further validated by EIS spectroscopy.[72] The superior charge separation effectiveness of **1-Tb** over metalloligand **1** was confirmed by its lower arc radius in the Nyquist plot (Fig. 6b). These results convincingly support the assertion that **1-Tb** is a highly efficient photocatalyst when compared to metalloligand **1**. The catalysis results proved the same.

Furthermore, from decay associated spectra of **1-Tb** (DAS; Fig. S117 and S118, ESI†), it is again evident that a decrease in the amplitude of the e-transfer component coincides well with an increase in the amplitude of the ~2 ns long decay component. This implies that the disappearance of the Tb^{2+} state is accompanied by the appearance of this long component, which is attributed to inter-system crossing (ISC) induced by the reduced Tb^{2+} ion (τ_{ISC} = time scale of inter-system crossing).[51,52,61] Thus, singlet excitons might have transitioned to triplet excitons, as illustrated by the TAS studies.[51,52,61] To understand this phenomenon better, phosphorescence spectra of **1** and **1-Tb** were measured and compared.[55] Ln-MOF **1-Tb** exhibited a strong phosphorescence peak at 519 nm (Fig. 6c), displaying a 67 nm red-shift with respect to the fluorescence peak at 452 nm. In fact, a longer lifetime of **1-Tb** (2.01 ms) further shows that the red-shifted emission is due to the triplet excitons (Fig. 6d).[55] In contrast, metalloligand **1** displayed a negligible intensity in its phosphorescence spectrum. A significant difference in the phosphorescence intensities of **1-Tb** and **1** (lifetime = 8.29 μs; Fig. 6d, inset) suggests that **1-Tb** generates triplet excitons that are not produced by the metalloligand alone. Hence, it is evident that the generation of the Tb^{2+} state facilitates singlet-to-triplet conversion followed by emission *via* phosphorescence to the singlet ground state. One should also take note of the fact that the amplitude of the rise component starts decreasing (*i.e.* becoming less negative) from around 500 nm and is lowest at 530 nm. This neatly coincides with the maximum of the phosphorescence spectrum and concomitant appearance of the ~2 ns ISC component. In summary, Fig. 6e presents a schematic representation of the ISC exhibited by Ln-MOF **1-Tb**.

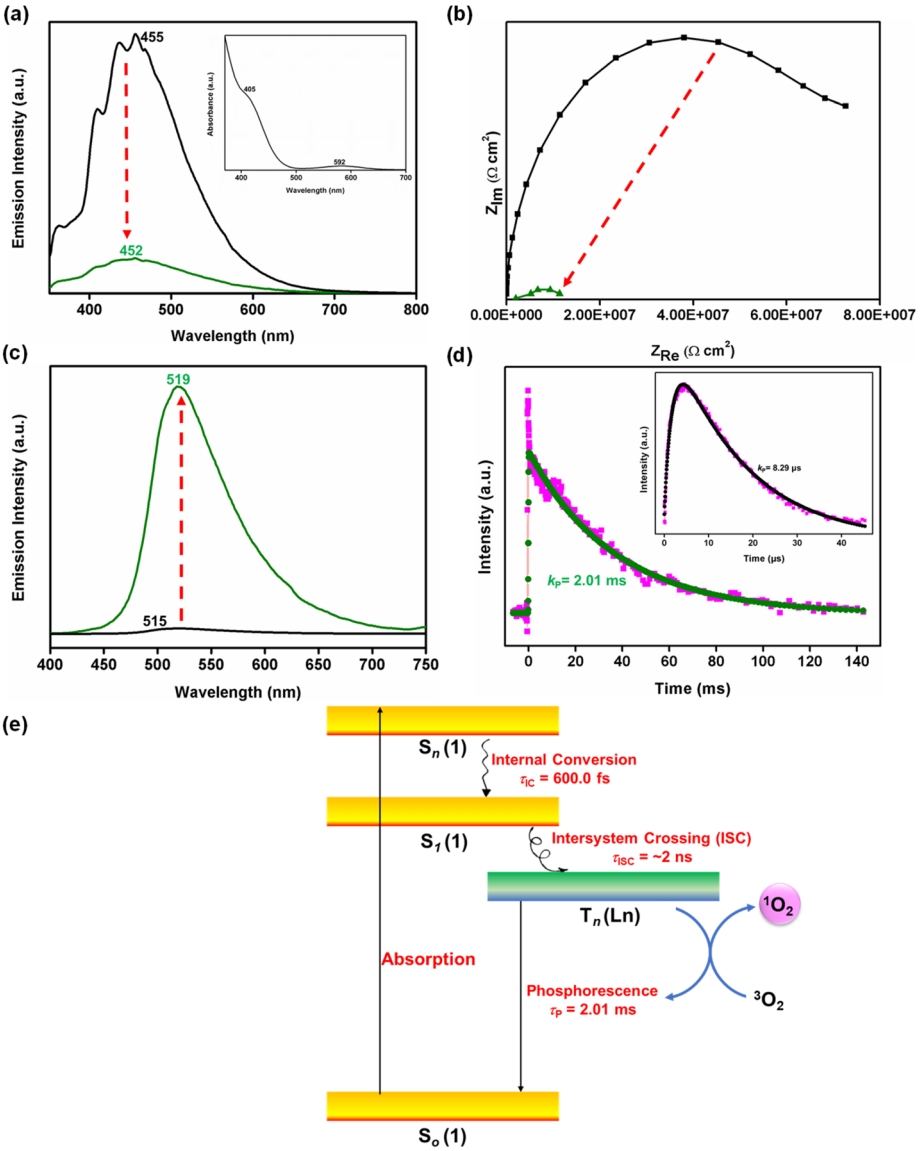

Fig. 6 (a) Photoluminescence spectra of **1** (black trace) and **1-Tb** (green trace), λ_{ex} = 350 nm. (Inset) UV-Vis diffuse reflectance spectrum of **1**. (b) EIS spectra of **1** (black trace) and **1-Tb** (green trace). (c) Phosphorescence spectra of **1** (black trace) and **1-Tb** (green trace), λ_{ex} = 400 nm. (d) Time-resolved phosphorescence spectrum of **1-Tb**. (Inset) Time-resolved phosphorescence spectrum of **1**. (e) Proposed Jablonski diagram for **1-Tb** illustrating intersystem crossing for the generation of singlet oxygen.

Single-crystal-to-single-crystal transformation: a zinc analogue (1-Zn) of 1-Tb

The heavy-atom like effect of a Ln^{3+} ion is anticipated to be the primary reason for the existence of triplet excitons in **1-Tb.**[73] To verify that the presence of a lanthanide ion such as Tb^{3+} can induce triplet-to-singlet oxygen conversion, we synthesized a non-heavy-metal analogue of **1-Tb**, **1-Zn**, by substituting Tb^{3+} by Zn^{2+} ions through a single-crystal-to-single-crystal transformation (SCSC) strategy.[74] The so-obtained **1-Zn** exhibited a complete replacement of Tb^{3+} ions by Zn^{2+} ions, as evidenced by various studies (Fig. 7 and S119–S121, ESI†). Conclusive evidence was obtained for the single crystal structure of **1-Zn**, which illustrated a clean and complete replacement of Tb^{3+} by Zn^{2+} ions (Fig. 7e and S123, ESI†).[75] In the crystal structure, for every two Tb^{3+} ions, three Zn^{2+} ions were found as a result of charge balance; although the space group remained the same ($P\bar{1}$) as that noted for **1-Tb**. The crystal structure of **1-Zn** showed major structural changes when compared to **1-Tb** (confirmed by PXRD studies, Fig. 7c). A set of three Zn^{2+} ions were coordinated by eight carboxylate groups emerging from six different metalloligands, resulting in a secondary building unit (SBU) of $[Zn_3(\mathbf{1})_6]$. In contrast, **1-Tb** showed the SBU's composition as $[Tb_2(\mathbf{1})_4]$. This clearly shows the replacement of two Tb^{3+} ions in **1-Tb** by three Zn^{2+} ions in **1-Zn**. Notably, protonated arylcarboxylic acid groups in **1-Tb** were fully deprotonated in **1-Zn** and were involved in coordination to the Zn^{2+} ions. Crystallographically, **1-Zn** is composed of fully deprotonated metalloligands connected to the Zn^{2+} ions, offering large cavities with

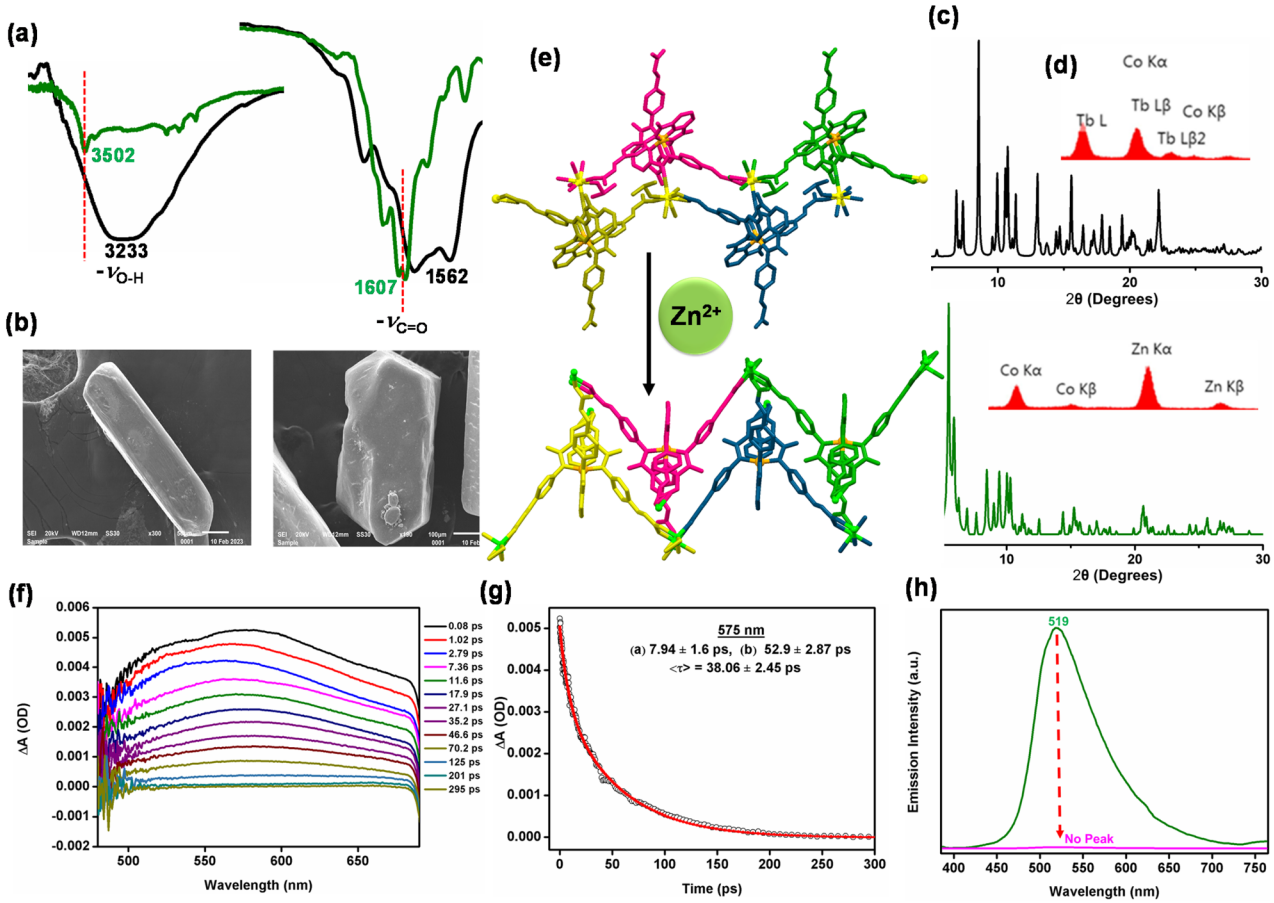

Fig. 7 A figure presenting multiple characterizations of **1-Zn** after its synthesis from **1-Tb** *via* single-crystal-to-single-crystal transformation. (a) FTIR spectra (black trace: **1-Tb**; green trace: **1-Zn**); (b) SEM images (left: **1-Tb**; right: **1-Zn**); (c) PXRD patterns (black trace: **1-Tb**; green trace: **1-Zn**); (d) EDX spectra (upper trace: **1-Tb**; lower trace: **1-Zn**); and (e) crystal structure of **1-Tb** and preliminary crystal structure of **1-Zn**. (f) Ultrafast transient absorption spectra of **1-Zn** (λ_{pump} = 375 nm) and (g) the corresponding decay kinetics (probed at the maximum of the excited state absorption spectra) of **1-Zn** at 575 nm. (h) Phosphorescence spectra of **1-Tb** (green trace) and **1-Zn** (pink trace), λ_{ex} = 380 nm.

dimensions of *ca* 9.4 × 19.2 Å^2. In fact, both the formation of a double chain structure and presence of large cavities in **1-Zn** are quite similar to those of **1-Tb**, thus justifying limited lattice changes as a result of SCSC. The presence of fully deprotonated metalloligands is also reflected in its FTIR spectrum (Fig. 7a), exhibiting sharp ν_{O-H} stretches for the lattice water molecules and well-defined ν_{COO} stretches for the carboxylate groups.

The newly synthesized **1-Zn** provided an excellent opportunity to test the heavy-atom effect of Tb^{3+} ions in **1-Tb** in generating the triplet excitons. Similar TA spectral experiments were carried out with **1-Zn** and the λ_{max}^{ESA} was noted to be 575 nm (Fig. 7f and g). The global analyses revealed the presence of two decay components of 7.5 ps (IC) and 53.3 ps (excited state decay), while no probe-dependent rise component was observed over the entire wavelength range (Fig. S124, ESI†). Therefore, the absence of both growth phase and long decay components suggests the absence of electron transfer and heavy-metal induced ISC, and the latter indicates the absence of phosphorescence.

Gratifyingly, the absence of a signal in the phosphorescence spectrum of **1-Zn** (Fig. 7h) indicates that in the absence of lanthanide ions, triplet exciton generation is not a favorable pathway. In fact, non-selective oxidation of benzyl alcohol to benzoic acid by using **1-Zn** pointed to the generation of strongly-oxidizing $^{\bullet}OH$ radicals. This was proved by the radical scavenger experiments involving isopropyl alcohol, a known scavenger for $^{\bullet}OH$ radicals, which completely inhibited the oxidation of benzyl alcohol.[9–14,25–28] Finally, the presence of $^{\bullet}OH$ radicals was confirmed by the selective oxidation of coumarin to 7-hydroxycoumarin, monitored by emission spectroscopy (Fig. S125 and S126, ESI†), which provided its concentration as *ca.* 10 μM.

In essence, it is proposed that upon photoexcitation, electron transfer (Table S10, ESI†) takes place from the Co^{3+}-based metalloligands (**1**; $\tau_{av(1)}$ = 24.50 ps) to the secondary Tb^{3+} ions in **1-Tb** ($\tau_{av(1\text{-}Tb)}$ = 1034.60 ps) generating the active Tb^{2+} sites which are responsible for the generation of triplet state excitons that activate triplet oxygen ($^3O_2$) to singlet oxygen ($^1O_2$). The singlet oxygen, thus generated, selectively catalyses the oxidation reactions. While evidence of a Tb^{2+} ion was obtained from the EPR spectrum, phosphorescence of **1-Tb** with a lifetime of ~2 ms further confirms ISC from the excited first singlet state (S_1) to the triplet manifold of the metalloligand induced by the

heavy Tb atom. However, only ligand **L** and only metalloligand **1** solely cannot induce the generation of triplet excitons as evident from both TAS and phosphorescence studies. Therefore, both **L** and **1** are not capable of catalyzing any visible-light mediated catalytic reaction. Similarly, the non-heavy-metal analogue of **1-Tb**, *i.e.* **1-Zn** ($\tau_{av(\mathbf{1\text{-}Zn})} = 38.06$ ps), cannot facilitate ISC that favours the generation of triplet excitons. In conclusion, a Co^{3+}-based metalloligand **1** functions as a photosensitizer to facilitate light absorption in the visible region while the catalytic reactions take place at the secondary Ln sites in the resultant Ln-MOFs.

Conclusions

This work presents Ln-MOFs based on an "integrated assembly approach" in which metalloligands performed the job of light absorption while long-range energy transfer was executed by the use of triplet excitons (*i.e.* Ln^{3+} ions). The Ln-MOFs were utilized for the selective oxidation of a wide range of alcohols and sulfides to their corresponding aldehydes/ketones and sulfoxides. The catalysis exhibited excellent substrate scope including pharmaceutically relevant compounds such as progesterone, estrone, and androstanolone; and detoxification of a mustard gas simulant. Nearly all catalytic reactions yielded quantitative products in less than 30 min reaction duration while using visible light. Transient absorption spectroscopy revealed a synergism between the discrete molecular components where electron transfer takes place from a metalloligand to the secondary lanthanide ions. The excited lanthanide ions with long triplet-state lifetimes, as confirmed by the phosphorescence studies, activated triplet $^3O_2$ to generate singlet $^1O_2$, as a mild and selective oxidant. The scavenger studies and $^1O_2$ traps further confirmed the photochemical generation of $^1O_2$, which illustrated its superiority in the selective oxidation of substrates without forming any over-oxidation product. Photoluminescence and electrochemical impedance spectroscopic studies showed that the coordination of Ln^{3+} ions to the metalloligands remarkably improved the charge-separation and electron-transport in the resultant Ln-MOFs, leading to their remarkably enhanced photocatalytic activity. The heavy-atom effect of a lanthanide ion in the generation of triplet excitons was confirmed by the synthesis of a non-heavy-metal analogue involving a zinc ion *via* a single-crystal-to-single-crystal transformation strategy. This work has demonstrated the novelty of the metalloligand strategy to tune the optical properties of the resultant materials. The utilization of an earth-abundant cobalt metal in the metalloligand is significant and a major shift from the conventional Ru- and Ir-based metalloligands. This work also opens up new avenues for developing metalloligand-based molecular architectures as the visible-light-driven photocatalysts for challenging organic transformations while relying on environmentally benign conditions.

Data availability

The necessary data pertaining to this article is available in the ESI.†

Author contributions

RuG designed the research work, conducted experiments, analyzed data, and drafted the first draft of the manuscript. Aashish and Upma performed the catalysis experiments. SM and PKC contributed to the TAS experiments, assisting with both experiments and data analysis. RG conceived the idea, coordinated research, acquired funds, and contributed to the review and drafting of the final manuscript. All authors read and approved the final version of the manuscript.

Conflicts of interest

The authors declare no competing financial interest.

Acknowledgements

RG gratefully acknowledges financial support from the Science and Engineering Research Board (CRG/2021/001700) and the Institution of Eminence, University of Delhi (FRP Project). RuG (CSIR, New Delhi), Aashish (CSIR, New Delhi), Upma (Inspire, DST, New Delhi), and SM (PMRF, MHRD, New Delhi) are grateful for their fellowships. PKC thanks the Department of Science and Technology, New Delhi (SR/FST/CS-II-027/2014) for providing funds for the ultrafast TA facility. The authors thank Dr Gulshan Kumar for his assistance in the synthetic work. The authors thank USIC of this university (for instrumental facilities), DST – SATHI facility at IIT – Delhi (for EPR and phosphorescence), IIT – Kanpur (for X-ray data collection), Prof. S. A. Hashmi (for BET), Prof. S. Murugavel (for EIS), and Prof. P. P. Chakraborty (for optical images).

Notes and references

1 X. Sun, S. Jiang, H. Huang, H. Li, B. Jia and T. Ma, Solar Energy Catalysis, *Angew. Chem., Int. Ed.*, 2022, **61**, e202204880.
2 X. Wang, K. Faungnawakij and M. Chareonpanich, Editorial: Photocatalysis – From Solar Power to Sustainable Chemical Production, *ChemCatChem*, 2019, **11**, 5838–5841.
3 S. Reischauer and B. Pieber, Emerging Concepts in Photocatalytic Organic Synthesis, *iScience*, 2021, **24**, 102209.
4 L. Xiong and J. Tang, Strategies and Challenges on Selectivity of Photocatalytic Oxidation of Organic Substances, *Adv. Energy Mater.*, 2021, **11**, 2003216.
5 G. D. Yadav, R. K. Mewada, D. P. Wagh and H. G. Manyar, Advances and Future Trends in Selective Oxidation Catalysis: A Critical Review, *Catal. Sci. Technol.*, 2022, **12**, 7245–7269.
6 D. M. Schultz and T. P. Yoon, Solar Synthesis: Prospects in Visible Light Photocatalysis, *Science*, 2014, **343**, 1239176.
7 D. Franchi and Z. Amara, Applications of Sensitized Semiconductors as Heterogeneous Visible-Light Photocatalysts in Organic Synthesis, *ACS Sustain. Chem. Eng.*, 2020, **8**, 15405–15429.

8 L. Marzo, S. K. Pagire, O. Reiser and B. König, Visible-Light Photocatalysis: Does It Make a Difference in Organic Synthesis?, *Angew. Chem., Int. Ed.*, 2018, **57**, 10034–10072.
9 L. Luo, T. Zhang, M. Wang, R. Yun and X. Xiang, Recent Advances in Heterogeneous Photo-Driven Oxidation of Organic Molecules by Reactive Oxygen Species, *ChemSusChem*, 2020, **13**, 5173–5184.
10 X. Yang and D. Wang, Photocatalysis: From Fundamental Principles to Materials and Applications, *ACS Appl. Energy Mater.*, 2018, **1**, 6657–6693.
11 X. Sun, C. Wang, D. Su, G. Wang and Y. Zhong, Application of Photocatalytic Materials in Sensors, *Adv. Mater. Technol.*, 2020, **5**, 1900993.
12 V. I. Parvulescu, F. Epron, H. Garcia and P. Granger, Recent Progress and Prospects in Catalytic Water Treatment, *Chem. Rev.*, 2022, **122**, 2981–3121.
13 U. Ulmer, T. Dingle, P. N. Duchesne, R. H. Morris, A. Tavasoli, T. Wood and G. A. Ozin, Fundamentals and Applications of Photocatalytic CO_2 Methanation, *Nat. Commun.*, 2019, **10**, 3169.
14 K. C. Christoforidis and P. Fornasiero, Photocatalytic Hydrogen Production: A Rift into the Future Energy Supply, *ChemCatChem*, 2017, **9**, 1523–1544.
15 C. Michelin and N. Hoffmann, Photosensitization and Photocatalysis—Perspectives in Organic Synthesis, *ACS Catal.*, 2018, **8**, 12046–12055.
16 W. Zhan, H. Gao, Y. Yang, X. Li and Q.-L. Zhu, Rational Design of Metal–Organic Framework-Based Materials for Photocatalytic CO_2 Reduction, *Adv. Energy Sustainability Res.*, 2022, **3**, 2200004.
17 L. Hong, R. Guo, Y. Yuan, X. Ji, Z. Lin, Z. Li and W. Pan, Recent Progress of Transition Metal Phosphides for Photocatalytic Hydrogen Evolution, *ChemSusChem*, 2021, **14**, 539–557.
18 M. Wang, K. Han, S. Zhang and L. Sun, Integration of Organometallic Complexes with Semiconductors and Other Nanomaterials for Photocatalytic H_2 Production, *Coord. Chem. Rev.*, 2015, **287**, 1–14.
19 S. Chandrasekaran, L. Yao, L. Deng, C. Bowen, Y. Zhang, S. Chen, Z. Lin, F. Peng and P. Zhang, Recent Advances in Metal Sulfides: From Controlled Fabrication to Electrocatalytic, Photocatalytic and Photoelectrochemical Water Splitting and Beyond, *Chem. Soc. Rev.*, 2019, **48**, 4178–4280.
20 S. Monro, K. L. Colón, H. Yin, J. I. Roque, P. Konda, S. Gujar, R. P. Thummel, L. Lilge, C. G. Cameron and S. A. McFarland, Transition Metal Complexes and Photodynamic Therapy from a Tumor-Centered Approach: Challenges, Opportunities, and Highlights from the Development of TLD1433, *Chem. Rev.*, 2019, **119**, 797–828.
21 S. Navalón, A. Dhakshinamoorthy, M. Álvaro, B. Ferrer and H. García, Metal–Organic Frameworks as Photocatalysts for Solar-Driven Overall Water Splitting, *Chem. Rev.*, 2023, **123**, 445–490.
22 H.-J. Son, C. Pac and S. O. Kang, Inorganometallic Photocatalyst for CO_2 Reduction, *Acc. Chem. Res.*, 2021, **54**, 4530–4544.
23 D. N. Tritton, F.-K. Tang, G. B. Bodedla, F.-W. Lee, C.-S. Kwan, K. C.-F. Leung, X. Zhu and W.-Y. Wong, Development and Advancement of Iridium(III)-Based Complexes for Photocatalytic Hydrogen Evolution, *Coord. Chem. Rev.*, 2022, **459**, 214390.
24 X. Yu, L. Wang and S. M. Cohen, Photocatalytic Metal–Organic Frameworks for Organic Transformations, *CrystEngComm*, 2017, **19**, 4126–4136.
25 M. Liras, M. Pintado-Sierra, M. Iglesias and F. A. Sánchez, Deprotection Strategy of a BODIPY Conjugated Porous Polymer to Obtain a Heterogeneous (Dipyrrin)(Bipyridine) Ruthenium(II) Visible Light Photocatalyst, *J. Mater. Chem. A*, 2016, **4**, 17274–17278.
26 R. Lindroth, K. L. Materna, L. Hammarström and C. -J Wallentin, Sustainable Ir-Photoredox Catalysis by Means of Heterogenization, *ACS Org. Inorg. Au*, 2022, **2**, 427–432.
27 J. C. Bawden, P. S. Francis, S. DiLuzio, D. J. Hayne, E. H. Doeven, J. Truong, R. Alexander, L. C. Henderson, D. E. Gómez, M. Massi, B. I. Armstrong, F. A. Draper, S. Bernhard and T. U. Connell, Reinterpreting the Fate of Iridium(III) Photocatalysts-Screening a Combinatorial Library to Explore Light-Driven Side-Reactions, *J. Am. Chem. Soc.*, 2022, **144**, 11189–11202.
28 P. Rana, R. Gaur, B. Kaushik, P. Rana, S. Yadav, P. Yadav, P. Sharma, M. B. Gawande and R. K. Sharma, Surface Engineered Iridium-Based Magnetic Photocatalyst Paving a Path towards Visible Light Driven C-H Arylation and Cyanation Reaction, *J. Catal.*, 2021, **401**, 297–308.
29 H.-C. Zhou, J. R. Long and O. M. Yaghi, Introduction to Metal–Organic Frameworks, *Chem. Rev.*, 2012, **112**, 673–674.
30 M. Ding, R. W. Flaig, H. -L Jiang and O. M. Yaghi, Carbon Capture and Conversion Using Metal—Organic Frameworks and MOF-Based Materials, *Chem. Soc. Rev.*, 2019, **48**, 2783–2828.
31 H.-C. Zhou and S. Kitagawa, Metal—Organic Frameworks (MOFs), *Chem. Soc. Rev.*, 2014, **43**, 5415–5418.
32 M. O'Keeffe and O. M. Yaghi, Deconstructing the Crystal Structures of Metal-Organic Frameworks and Related Materials into Their Underlying Nets, *Chem. Rev.*, 2012, **112**, 675–702.
33 H. Furukawa, N. Ko, Y. B. Go, N. Aratani, S. B. Choi, E. Choi, A. O. Yazaydin, R. Q. Snurr, M. O'Keeffe, J. Kim and O. M. Yaghi, Ultrahigh Porosity in Metal-Organic Frameworks, *Science*, 2010, **329**, 424–428.
34 A. Bavykina, N. Kolobov, I. S. Khan, J. A. Bau, A. Ramirez and J. Gascon, Metal–Organic Frameworks in Heterogeneous Catalysis: Recent Progress, New Trends, and Future Perspectives, *Chem. Rev.*, 2020, **120**, 8468–8535.
35 M. Y. Masoomi, A. Morsali, A. Dhakshinamoorthy and H. Garcia, Mixed-Metal MOFs: Unique Opportunities in Metal—Organic Framework (MOF) Functionality and Design, *Angew. Chem., Int. Ed.*, 2019, **58**, 15188–15205.
36 G. Kumar, G. Kumar and R. Gupta, Effect of Pyridyl Donors from Organic Ligands versus Metalloligands on Material Design, *Inorg. Chem. Front.*, 2021, **8**, 1334–1373.
37 R. Gupta, G. Kumar and R. Gupta, Encapsulation-Led Adsorption of Neutral Dyes and Complete

Photodegradation of Cationic Dyes and Antipsychotic Drugs by Lanthanide-Based Macrocycles, *Inorg. Chem.*, 2022, **61**, 7682–7699.

38 S. Pachisia and R. Gupta, Tailored Inorganic-Organic Architectures via Metalloligands, *Chem. Rec.*, 2022, **22**, e202200121.

39 Z.-H. Yan, M.-H. Du, J. Liu, S. Jin, C. Wang, G.-L. Zhuang, X.-J. Kong, L.-S. Long and L.-S. Zheng, Photo-Generated Dinuclear $\{Eu(II)\}_2$ Active Sites for Selective CO_2 Reduction in a Photosensitizing Metal-Organic Framework, *Nat. Commun.*, 2018, **9**, 3353.

40 N.-Y. Huang, H. He, S. Liu, H.-L. Zhu, Y.-J. Li, J. Xu, J.-R. Huang, X. Wang, P.-Q. Liao and X.-M. Chen, Electrostatic Attraction-Driven Assembly of a Metal–Organic Framework with a Photosensitizer Boosts Photocatalytic CO_2 Reduction to CO, *J. Am. Chem. Soc.*, 2021, **143**, 17424–17430.

41 R. Jaryal, R. Kumar and S. Khullar, Mixed Metal-Metal Organic Frameworks (MM-MOFs) and Their Use as Efficient Photocatalysts for Hydrogen Evolution from Water Splitting Reactions, *Coord. Chem. Rev.*, 2022, **464**, 214542.

42 J. Gao, Q. Huang, Y. Wu, Y.-Q. Lan and B. Chen, Metal–Organic Frameworks for Photo/Electrocatalysis, *Adv. Energy Sustainability Res.*, 2021, **2**, 2100033.

43 Z.-B. Fang, T.-T. Liu, J. Liu, S. Jin, X.-P. Wu, X.-Q. Gong, K. Wang, Q. Yin, T.-F. Liu, R. Cao and H.-C. Zhou, Boosting Interfacial Charge-Transfer Kinetics for Efficient Overall CO_2 Photoreduction via Rational Design of Coordination Spheres on Metal–Organic Frameworks, *J. Am. Chem. Soc.*, 2022, **142**, 12515–12523.

44 K. Fan, W.-X. Nie, L.-P. Wang, C.-H. Liao, S.-S. Bao and L.-M. Zheng, Defective Metal–Organic Frameworks Incorporating Iridium-Based Metalloligands: Sorption and Dye Degradation Properties, *Chem.–Eur. J.*, 2017, **23**, 6615–6624.

45 X. Feng, Y. Pi, Y. Song, C. Brzezinski, Z. Xu, Z. Li and W. Lin, Metal–Organic Frameworks Significantly Enhance Photocatalytic Hydrogen Evolution and CO_2 Reduction with Earth-Abundant Copper Photosensitizers, *J. Am. Chem. Soc.*, 2020, **142**, 690–695.

46 M.-H. Xie, X.-L. Yang, C. Zou and C.-D. Wu, A SnIV–Porphyrin-Based Metal–Organic Framework for the Selective Photo-Oxygenation of Phenol and Sulfides, *Inorg. Chem.*, 2011, **50**, 5318–5320.

47 M. S. Deenadayalan, N. Sharma, P. K. Verma and C. M. Nagaraja, Visible-Light-Assisted Photocatalytic Reduction of Nitroaromatics by Recyclable Ni(II)-Porphyrin Metal–Organic Framework (MOF) at RT, *Inorg. Chem.*, 2016, **55**, 5320–5327.

48 J. Guo, Y.-Z. Fan, Y.-L. Lu, S.-P. Zheng and C.-Y. Su, Visible-Light Photocatalysis of Asymmetric [2+2] Cycloaddition in Cage-Confined Nanospace Merging Chirality with Triplet-State Photosensitization, *Angew. Chem., Int. Ed.*, 2020, **59**, 8661–8669.

49 Y.-Z. Chen, Z. U. Wang, H. Wang, J. Lu, S.-H. Yu and H.-L. Jiang, Singlet Oxygen-Engaged Selective Photo-Oxidation over Pt Nanocrystals/Porphyrinic MOF: The Roles of Photothermal Effect and Pt Electronic State, *J. Am. Chem. Soc.*, 2017, **139**, 2035–2044.

50 Y. Zhang, W. Schilling, D. Riemer and S. Das, Metal-Free Photocatalysts for the Oxidation of Non-Activated Alcohols and the Oxygenation of Tertiary Amines Performed in Air or Oxygen, *Nat. Protoc.*, 2020, **15**, 822–839.

51 H.-P. Liang, Q. Chen and B.-H. Han, Cationic Polycarbazole Networks as Visible-Light Heterogeneous Photocatalysts for Oxidative Organic Transformations, *ACS Catal.*, 2018, **8**, 5313–5322.

52 Q.-Y. Wang, J. Liu, M. Cao, J.-H. Hu, R. Pang, S. Wang, M. Asad, Y.-L. Wei and S.-Q. Zang, Aminal-Linked Porphyrinic Covalent Organic Framework for Rapid Photocatalytic Decontamination of Mustard-Gas Simulant, *Angew. Chem., Int. Ed.*, 2022, **61**, e202207130.

53 W. Zhang, B. Li, H. Ma, L. Zhang, Y. Guan, Y. Zhang, X. Zhang, P. Jing and S. Yue, Combining Ruthenium(II) Complexes with Metal–Organic Frameworks to Realize Effective Two-Photon Absorption for Singlet Oxygen Generation, *ACS Appl. Mater. Interfaces*, 2016, **8**, 21465–21471.

54 Y. Hao, B. M. Liu, T. F. Bennett, C. G. Monsour, M. Selke and Y. Liu, Determination of Singlet Oxygen Quantum Yield of a Porphyrinic Metal–Organic Framework, *J. Phys. Chem. C*, 2021, **125**, 7392–7400.

55 R. Zhang, Y. Liu, Z. Wang, P. Wang, Z. Zheng, X. Qin, X. Zhang, Y. Dai, M.-H. Whangbo and B. Huang, Selective Photocatalytic Conversion of Alcohol to Aldehydes by Singlet Oxygen over Bi-Based Metal-Organic Frameworks under UV–Vis Light Irradiation, *Appl. Catal., B*, 2019, **254**, 463–470.

56 Both Ln-MOFs also contained a number of lattice solvent molecules, **1-Tb** having one DMSO and eight water molecules while **1-Eu** with two water molecules. The presence of such lattice solvent molecules was supported by both FTIR spectral and thermal (TGA and DSC) studies (Fig. S15 and S16, ESI†).

57 L. Feng, K.-Y. Wang, X.-L. Lv, T.-H. Yan and H.-C. Zhou, Hierarchically Porous Metal—Organic Frameworks: Synthetic Strategies and Applications, *Natl. Sci. Rev.*, 2020, **7**, 1743–1758.

58 K. Sivula, Mott–Schottky Analysis of Photoelectrodes: Sanity Checks Are Needed, *ACS Energy Lett.*, 2021, **6**, 2549–2551.

59 P. Makuła, M. Pacia and W. Macyk, How To Correctly Determine the Band Gap Energy of Modified Semiconductor Photocatalysts Based on UV–Vis Spectra, *J. Phys. Chem. Lett.*, 2018, **9**, 6814–6817.

60 J. T. Schneider, D. S. Firak, R. R. Ribeiro and P. Peralta-Zamora, Use of Scavenger Agents in Heterogeneous Photocatalysis: Truths, Half-Truths, and Misinterpretations, *Phys. Chem. Chem. Phys.*, 2020, **22**, 15723–15733.

61 R.-Q. Xia, J. Zheng, R.-J. Wei, J. He, D.-Q. Ye, M.-D. Li, G.-H. Ning and D. Li, Strong Visible Light-Absorbing BODIPY-Based Cu(I) Cyclic Trinuclear Sensitizer for Photocatalysis, *Inorg. Chem. Front.*, 2022, **9**, 2928–2937.

62 Y. Nosaka and A. Y. Nosaka, Generation and Detection of Reactive Oxygen Species in Photocatalysis, *Chem. Rev.*, 2017, **117**, 11302–11336.

63 Y. Zhang, W. Schiling, D. Riemer and S. Das S, Metal-free photocatalysts for the oxidation of non-activated alcohols and the oxygenation of tertiary amines performed in air or oxygen, *Nat. Protoc.*, 2020, **15**, 822–839.

64 Q. Xiao, Z. Liu, A. Bo, S. Zavahir, S. Sarina, S. Bottle, J. D. Riches and H. Zhu, Catalytic Transformation of Aliphatic Alcohols to Corresponding Esters in O_2 under Neutral Conditions Using Visible-Light Irradiation, *J. Am. Chem. Soc.*, 2015, **137**, 1956–1966.

65 Z. Wang, L. Zeng, C. He and C. Duan, Photocatalytic C–H Activation with Alcohol as a Hydrogen Atom Transfer Agent in a 9-Fluorenone Based Metal–Organic Framework, *ACS Appl. Mater. Interfaces*, 2021, **13**, 25898–25905.

66 W. Huang, B. C. Ma, H. Lu, R. Li, L. Wang, K. Landfester and K. A. I. Zhang, Visible-Light-Promoted Selective Oxidation of Alcohols Using a Covalent Triazine Framework, *ACS Catal.*, 2017, **7**, 5438–5442.

67 Y. Wei, J. Zhang, Q. Zheng, J. Miao, J. Alvarez, J. PedroJ and M. Long, Quantification of Photocatalytically-Generated Hydrogen Peroxide in the Presence of Organic Electron Donors: Interference and Reliability Considerations, *Chemosphere*, 2021, **279**, 130556.

68 Z. Sroka and W. Cisowski, Hydrogen Peroxide Scavenging, Antioxidant and Anti-Radical Activity of Some Phenolic Acids, *Food Chem. Toxicol.*, 2003, **41**, 753–758.

69 T. J. Miao and J. Tang, Characterization of Charge Carrier Behavior in Photocatalysis Using Transient Absorption Spectroscopy, *J. Chem. Phys.*, 2020, **152**, 194201.

70 M. Kumar and S. K. Gupta, An Insight into Optical Spectroscopy of Intense Green Emitting $ZnAl_2O_4$:Tb^{3+} Nanoparticles: Photo, Thermally Stimulated Luminescence and EPR Study, *J. Lumin.*, 2015, **168**, 151–157.

71 W. Gao, J. Lu, S. Zhang, X. Zhang, Z. Wang, W. Qin, J. Wang, W. Zhou, H. Liu and Y. Sang, Suppressing Photoinduced Charge Recombination via the Lorentz Force in a Photocatalytic System, *Adv. Sci.*, 2019, **6**, 1901244.

72 C. Pan, J. Xu, Y. Wang, D. Li and Y. Zhu, Dramatic Activity of C_3N_4/$BiPO_4$ Photocatalyst with Core/Shell Structure Formed by Self-Assembly, *Adv. Funct. Mater.*, 2012, **22**, 1518–1524.

73 A. Balamurugan, A. K. Gupta, R. Boomishankar, M. Lakshmipathi Reddy and M. Jayakannan, Heavy Atom Effect Driven Organic Phosphors and Their Luminescent Lanthanide Metal-Organic Frameworks, *Chempluschem*, 2013, **78**, 737–745.

74 W. Chen, Z. Wang, Q. Wang, K. El-Yanboui, K. Tan, H. M. Barkholtz, D.-J. Liu, P. Cai, L. Feng, Y. Li, J.-S. Qin, S. Yuan, D. Sun and H.-C. Zhou, Monitoring the Activation of Open Metal Sites in [$Fe_xM_{3-x}(_3$-O)] Cluster-Based Metal–Organic Frameworks by Single-Crystal X-Ray Diffraction, *J. Am. Chem. Soc.*, 2023, **145**, 4736–4745.

75 Crystal quality of **1-Zn**, obtained via single-crystal-to-single-crystal transformation from **1-Tb**, was not very good. Although one such crystal diffracted and resulted in data collection but only allowed a partial structure solution. Crystal data: cell = triclinic, space group = $P\bar{1}$, a = 17.271(6) Å, b = 17.499(6) Å, c = 18.473(6) Å, α = 107.044(8)°, β = 115.156(8)°, γ = 95.744(9)°, V = 4665.86, Z = 1.